JMEPEG (2020) 29:7662–7677
https://doi.org/10.1007/s11665-020-05220-y

1059-9495/$19.00

Warm Tensile Deformation and Fracture Behavior of AZ31 Magnesium Alloy Sheets Processed by Constrained Groove Pressing

Zongshen Wang, Kangning Wang, Xiebin Wang, Tao Wang, Lihua Zhu, and Yanjin Guan

Submitted: 11 June 2020 / Revised: 20 September 2020 / Accepted: 21 September 2020 / Published online: 26 October 2020

Constrained groove pressing (CGP), as a promising severe plastic deformation method suitable for processing sheet metals, was applied to AZ31 magnesium alloy sheets, and ultra-fine grained structure was achieved after two passes of CGP at 473 K. A bimodal structure was also developed due to partial dynamic recrystallization (DRX) and deformation homogeneity. Tensile tests at temperatures from room temperature to 523 K and strain rates from 1×10^{-4} to 1×10^{-1} s^{-1} were conducted to the processed alloy sheets, and their tensile deformation and fracture behavior were investigated in this work. The maximum elongation to failure of 38.7% is achieved at 1×10^{-4} s^{-1} and 473 K, and the yield strength and tensile strength are 37.0 and 43.0 MPa, respectively. The strain hardening ability increases gradually with increasing strain rate at elevated temperatures, and its dependence on strain rate is more significant at lower temperatures. The strain rate sensitivity coefficient gradually increases with increasing temperature, and the relatively high values of ~ 0.17 and ~ 0.14 are obtained at 473 and 523 K, respectively, indicating the absence of superplastic behavior. The fracture morphology shows that with increasing temperature, the fracture mode changes from brittle fracture to ductile fracture, which is closely related to the microstructural evolution during tensile deformation. The grain coarsening at 523 K may result in the slight decreases of elongation to failure and strain rate sensitivity coefficient as well as the recovery of strain hardening exponent. The apparent activation energy at 423-523 K is estimated to be 68.8-105.5 kJ/mol. Conclusively, DRX and grain growth should be the dominant mechanism accounting for the warm tensile deformation of AZ31 magnesium alloy sheets processed by CGP, while grain boundary sliding mechanism may contribute little, due to the developed bimodal structure during CGP and the relatively low temperatures for the tensile tests.

Keywords AZ31 magnesium alloy, bimodal structure, constrained groove pressing, fracture behavior, severe plastic deformation, warm tensile deformation

1. Introduction

Reduction of mass is one of the most effective and least costly ways to reduce fuel consumption and exhaust emission of vehicles (Ref 1). Magnesium alloys are the lightest commercialized metallic structural materials widely used in aerospace, automobile and construction industries (Ref 2). However, the hexagonal close packed (HCP) crystal structure and insufficient slip systems result in low ductility and poor formability of magnesium alloys at room temperature (RT). As a result, the forming of magnesium alloys is usually performed at elevated temperatures, which greatly increases the manufacturing cost. Therefore, lowering the processing temperature is highly desirable to achieve complex shape forming and expand the application scope of magnesium alloys. Moreover, poor corrosion resistance is also revealed in magnesium alloys, owing to their high chemical activity and the lack of protective passive oxide film (Ref 3-5). On one hand, the intrinsic dissolution tendency of magnesium only weakly inhibited by corrosion product film leads to the poor corrosion resistance of magnesium alloys in aqueous solutions (Ref 3). On the other hand, the presence of impurities and second phases usually causes local galvanic acceleration of corrosion by acting as local cathodes. Thus, difficulties in fabricating components with good performance have greatly limited the application and development of magnesium alloys in a wider range, and many attempts have been performed to resolve these restrictions.

Severe plastic deformation (SPD) is a powerful technique to improve the engineering properties of magnesium alloys by fabricating ultra-fine grained (UFG) structure in materials (Ref 6). It is widely recognized that polycrystalline materials with average grain sizes smaller than about 1 μm can be defined as UFG materials (Ref 7). Thus, microstructure with grain sizes lying within submicrometer (100-1000 nm) and nanometer (< 100 nm) ranges can be defined as an UFG structure. As an alternative to the nanopowder compacting methods, SPD overcomes some difficulties associated with residual porosity in compacted samples, impurities from ball milling and processing of large scale billets, and various SPD methods

Zongshen Wang, Kangning Wang, and **Lihua Zhu**, School of Mechanical Engineering, Shandong University of Technology, Zibo 255000, People's Republic of China; **Xiebin Wang**, School of Materials Science and Engineering, Shandong University, Jinan 250061, People's Republic of China; and Suzhou Institute of Shandong University, Suzhou 215123, People's Republic of China; and **Tao Wang** and **Yanjin Guan**, School of Materials Science and Engineering, Shandong University, Jinan 250061, People's Republic of China. Contact e-mail: wangzsh@sdut.edu.cn.

have been developed up to now (Ref 8). Of these, equal-channel angular pressing (ECAP) (Ref 9), high-pressure torsion (HPT) (Ref 10) and accumulative roll-bonding (ARB) (Ref 11, 12) are the most common and well-investigated SPD methods (Ref 13). Among them, only ARB is available for processing plate shaped materials or sheet metals since the typical shape and size of samples for ECAP and HPT are very limited (Ref 12). However, during ARB, the problems of fracture and edge cracks of the sheets as well as the strict requirements for surface conditions and atmosphere hinder its further development. As a novel and promising SPD method, constrained groove pressing (CGP) is simple and effective, and it is more suitable for producing UFG sheet metals, compared with ARB and other SPD methods (Ref 14, 15). During CGP, a set of asymmetrical groove dies and a set of flat dies are utilized to perform alternate groove pressings and flattenings to the sheet sample. By virtue of the constraint from the die walls and the asymmetry of the groove dies, theoretically pure shear deformation is uniformly accumulated into the sample without any distinct changes in its initial dimensions. Then, by repeating this process, a large amount of plastic strain can be introduced into the materials and an UFG structure is expected to be achieved. Until now, CGP has been successfully applied to grain refinement and property enhancement of various pure metals and alloys (Ref 15).

Nevertheless, most of the experimental materials investigated in previous works on CGP have good ductility such as aluminum and its alloys (Ref 16-20), copper and its alloys (Ref 21-23) and low carbon steel (Ref 24-26), and are generally processed at RT. Only several investigations on CGP of materials with poor formability like magnesium alloys have been reported recently. Ratna Sunil et al. firstly investigated the influence of microstructural evolution and surface features introduced by CGP on wettability, corrosion resistance, bioactivity and cell adhesion of AZ31 magnesium alloy (Ref 27). CGP was proved to be a potential method to improve bioactivity and control degradation of magnesium alloys for their implant application. Fong et al. numerically and experimentally investigated the effects of strain path and deformation temperature on CGP of AZ31 magnesium alloy sheets and found that CGP using an orthogonal pressing at every cycle and at a progressively decreasing temperature was effective for fabrication of UFG structure (Ref 28). Then, isothermal annealing from 473 K to 623 K was performed by Fong et al. to examine the thermal stability of the magnesium alloy sheets processed by CGP (Ref 29). The phenomenon of abnormal grain growth occurred at 623 K resulted from an increase in non-basal grains by consuming basal grains. UFG metallic materials usually exhibit high strength at RT and superplastic behavior at higher temperatures. In order to expand the application scope of magnesium alloys, their warm tensile deformation behavior at different temperatures and strain rates have drawn much attention of researchers. Fong et al. further investigated the tensile flow behavior at high temperatures of AZ31 magnesium alloy sheets after CGP and short time post-annealing (Ref 30). It was revealed that the dominant deformation process was climb-controlled dislocation creep associated with lattice diffusion. Hoseini-Athar et al. studied the microstructural evolution and superplastic behavior of Mg-Gd alloy sheets processed by CGP and found that the deformation mechanism in the superplastic regime was related to grain boundary sliding (GBS) controlled by grain boundary diffusion (Ref 31). It can be found that CGP shows great potential for improving the formability of magnesium alloy sheets. Nevertheless, limited works on tensile flow behavior under different conditions of magnesium alloy sheets processed by CGP have been reported until now, and the dominant deformation mechanism is still not very clear.

Recently, the authors developed a high-efficiency experimental setup with heating systems to perform high-temperature CGP on hard-to-deform materials, and the effects of pass number and deformation temperature on microstructure and mechanical properties of AZ31 magnesium alloy sheets during CGP were investigated systematically (Ref 32). Further in the present work, the warm tensile deformation and fracture behavior of AZ31 magnesium alloy sheets processed by CGP were investigated by uniaxial tensile tests under different deformation conditions. The influences of deformation temperature and strain rate on the flow behavior, strain hardening ability, strain rate sensitivity, microstructural evolution and fracture morphology of the materials were discussed in details, and the relevant mechanism was also analyzed. In other words, the objective of this work is to evaluate the influence of two passes of CGP at 473 K, as a pretreatment process, on the tensile deformation and fracture behavior of AZ31 magnesium alloy sheets at moderately high temperatures from RT to 523 K and strain rates from 1×10^{-4} s^{-1} to 1×10^{-1} s^{-1} and examine their formability improvement under these conditions introduced by CGP.

2. Experimental Materials and Procedure

The experimental materials were the hot-rolled AZ31 magnesium alloy sheets with dimensions of $100 \times 100 \times 2$ mm^3, and their chemical compositions are listed in Table 1. After annealed at 573 K for 1 h, the alloy sheets were processed by the experimental setup utilized in our previous work, and more details can be found elsewhere (Ref 32). As already reported, although relatively superior tensile properties were achieved at 473 K, micro-cracks and crack growth began to appear during the second pass, and more passes would induce not further enhanced properties but failure to the materials. Thus, in this work, only two passes of CGP were conducted to the alloy sheets at 473 K with a groove angle of 45° and a groove width of 2 mm. The effective strain accumulation during one pass of CGP is illustrated in Fig. 1, and using the above design of groove dies, theoretically an effective strain of about 1.16 will be uniformly accumulated into the sheet sample after one pass including four pressings (Ref 33). A constant pressing speed of 5 mm/min was used in this experiment, and molybdenum disulfide was adopted as the lubricant to reduce the friction between the contacting surfaces of the dies and sheet sample.

Optical microscope, transmission electron microscope (TEM) and x-ray diffraction (XRD) were employed to reveal

Table 1 Chemical compositions of AZ31 magnesium alloy used in this experiment (wt.%)

Al	Zn	Mn	Fe	Cu	Si	Mg
3.083	0.842	0.312	0.002	0.001	0.024	Balance

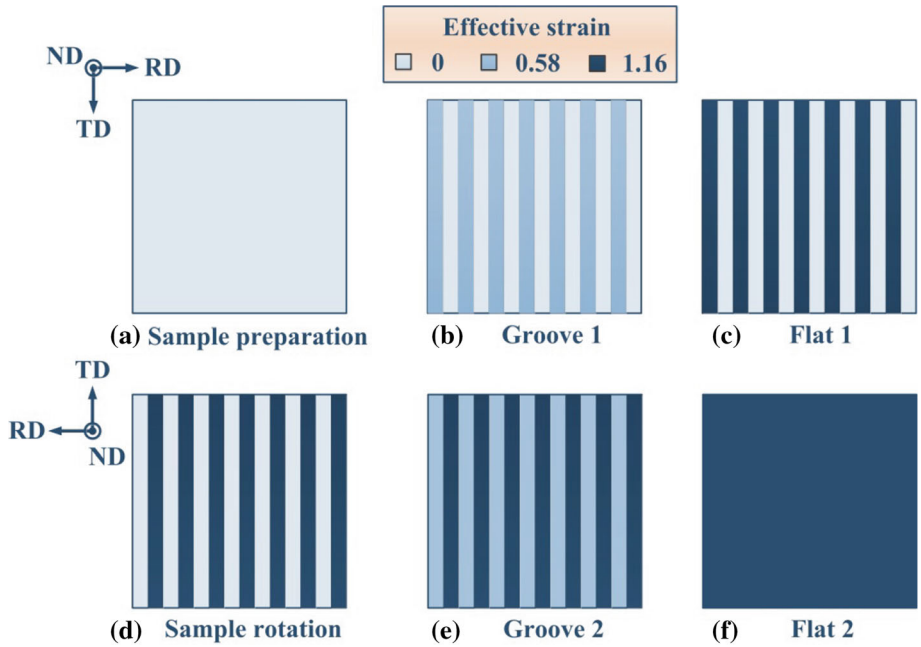

Fig. 1 Schematic illustration of effective strain accumulation during one pass of CGP: (a) Sample preparation, (b) Groove 1, (c) Flat 1, (d) Sample rotation, (e) Groove 2 and (f) Flat 2. Note: RD, TD and ND represent rolling direction, transverse direction and normal direction of the sheet sample, respectively

the microstructure of the magnesium alloy sheets before and after CGP. Specimens for optical microstructure observation were prepared by mechanical grinding and polishing, followed by etching with a picronitric acid solution. TEM specimens were cut from the central region of the sheet samples and traditionally prepared by mechanical polishing and ion thinning. TEM observation and selected-area electron diffraction (SAED) were carried out with an FEI Tecnai G2 F20 S-TWIN field emission TEM operated at 200 kV. As a supplementary of microstructural characterization, XRD was also performed to the sheet samples before and after CGP by a DMAX-2500PC diffractionmeter using Cu K_α radiation with the sample tilt angle ranging from 30° to 85°.

In order to systematically explore the flow behavior of the magnesium alloy sheets processed after a two-pass CGP, uniaxial tensile tests were carried out on a CMT-30 electronic universal testing machine within the temperature range of RT (298 K)-523 K and strain rate range of 1×10^{-4}-1×10^{-1} s^{-1}. Tensile specimens with gage dimensions of $15 \times 3 \times 2$ mm^3 were machined, and the gage length was aligned along the rolling direction (RD) of the sheets which was perpendicular to the groove direction of the dies when pressing, as shown in Fig. 1. To further examine the fracture behavior and deformation mechanism of tensile specimens, the fracture surfaces were observed by an FEI Apreo field emission scanning electron microscope (SEM).

3. Results and Discussion

3.1 UFG Structure of the AZ31 Magnesium Alloy Sheets Fabricated by CGP

In this experiment, two passes of CGP were conducted to the as-annealed AZ31 magnesium alloy sheets at 473 K. The microstructural evolution of the materials during CGP is shown in Fig. 2. Coarse and equiaxed grains are observed in the optical microstructure of the as-annealed materials, and the average grain size is about 11.3 μm, as shown in Fig. 2(a). Then, partial dynamic recrystallization (DRX) happens after one pass of CGP, and numerous small DRX grains form along the initial grain boundaries, as indicated by white arrows in Fig. 2(b). After two passes, the extent of DRX is enhanced, and more coarse grains are consumed by fine DRX grains. Further grain refinement is achieved by DRX with a final average grain size of around 3.2 μm although some coarse grains still exist in the deformed microstructure, suggesting that the bimodal structure is preserved eventually, as seen in Fig. 2(c). According to the grain refinement model of magnesium alloys during ECAP proposed by Figueiredo and Langdon, a bimodal structure will appear when the initial grain size of the materials is larger than a critical value due to the occurrence of DRX (Ref 34-36). During DRX, the fine grains preferentially nucleate along the initial boundaries of the coarse grains and the twin boundaries in a necklace-like pattern, resulting from the high stress concentration at the boundaries and subsequent activation of both basal and non-basal slip systems, while the inner cores of the coarse grains may not be refined (Ref 36). This induced bimodal grain size distribution in the deformed microstructure is defined as a bimodal structure. Besides the initial grain size, the size of fine DRX grains also greatly affects the microstructural evolution of magnesium alloys during SPD (Ref 36). Thus, when processed at a relatively low temperature of 473 K, both the size and volume fraction of new DRX grains are very small, leading to the occurrence and preservation of the bimodal structure even after two passes of CGP (Ref 32). Meanwhile, lots of twins can also be found in the deformed microstructure to accommodate plastic deformation at this temperature, as indicated by yellow arrows in Fig. 2(b) and (c). It is believed that the induced deformation inhomogeneity

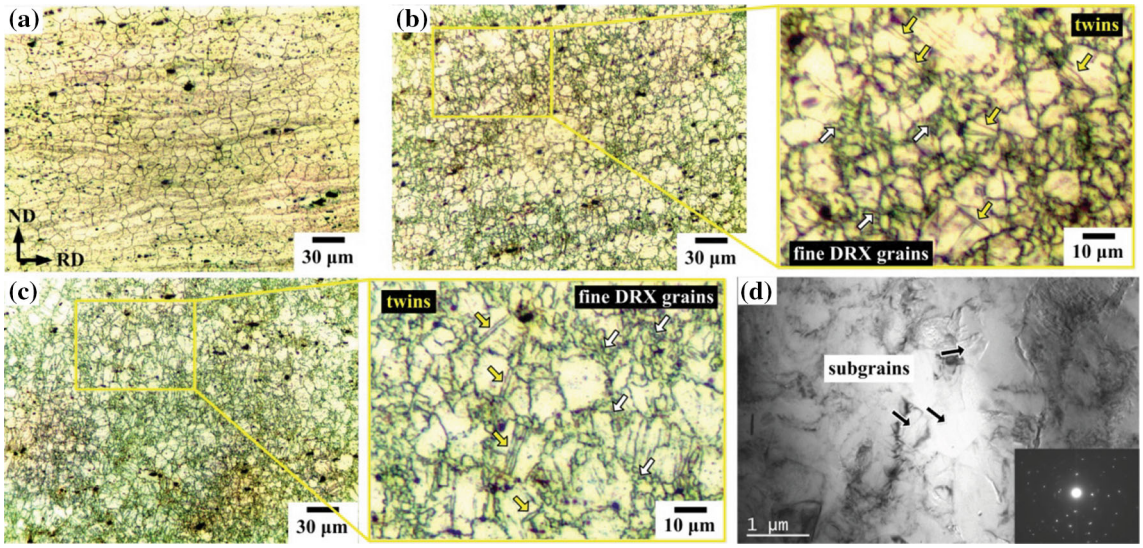

Fig. 2 Microstructural evolution of AZ31 magnesium alloy sheets during CGP at 473 K: Optical micrographs of (a) as-annealed, (b) one pass and (c) two passes, TEM micrograph with SAED patterns of (d) two passes. Note: Twins, fine DRX grains and subgrains are indicated by yellow, white and black arrows, respectively

during CGP can be improved by increasing plastic strain, but it still exists after the process (Ref 37, 38). This may also account for the microstructural evolution of the materials in this situation. As shown in Fig. 2(d), subgrains of about 0.5 μm could be observed with relatively low misorientation angles demonstrated by the slightly diffused SAED patterns, suggesting the achievement of an UFG structure. A mixed microstructure of DRX grains and deformed (sub)grains may also be developed due to partial DRX and deformation homogeneity (Ref 39). Thus, an UFG structure could be found from both the fine DRX grains and the substructured/deformed (sub)grains in the bimodal structure, and the subgrains indicated in Fig. 2(d) are more likely related to the latter. A detailed analysis about this phenomenon has been carried out by the authors in another submitted work about the effect of strain path on CGP of AZ31 magnesium alloy sheets.

As well known, TEM can provide a direct image for the microstructural features. However, grain overlapping leads to uncertainty and the reliability also depends on whether the limited thin area is a representative of the original microstructure of the entire sample. Thus, as a complement for TEM observation, XRD patterns of the AZ31 magnesium alloy sheets before and after processed by two passes of CGP are presented in Fig. 3, because XRD analysis has the advantages of averaging over a much larger area of the sample and ease of sample preparation (Ref 24). Firstly, as seen in Fig. 3, the as-annealed sheets exhibit a strong (0001) basal texture and, after CGP, its intensity is slightly decreased, while the intensity of (10-10) and (10-11) peaks goes up obviously. Secondly, peak broadening is observed after CGP, suggesting a decreased crystallite size. As well known, the broadening of diffraction peaks induced by increased crystal imperfectness is associated with relevant microstructural changes (Ref 40). The crystallite size and lattice microstrain of polycrystalline materials after SPD can be estimated by assuming the peak broadening are mainly caused by the changes in crystallite size and lattice distortion during straining (Ref 41). Various methods have been employed to compare the deviation of XRD patterns of the materials after SPD with the perfect crystal diffraction patterns.

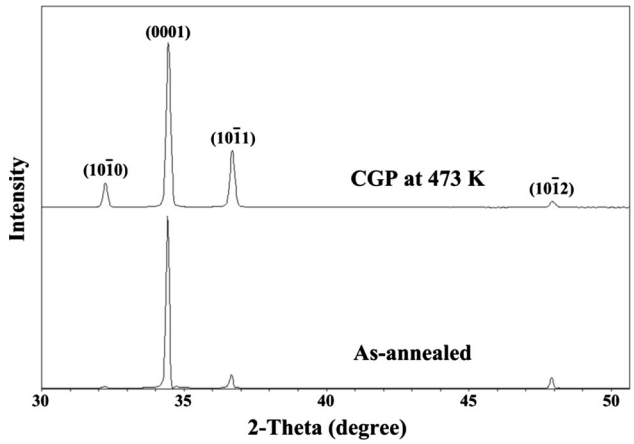

Fig. 3 XRD patterns of AZ31 magnesium alloy sheets before and after CGP

Of these, Williamson-Hall method is the simplest one and expressed by the following equation (Ref 42):

$$B\cos\theta = \frac{k\lambda}{t} + f(\varepsilon)\sin\theta \qquad \text{(Eq 1)}$$

where B is the integral breadth of XRD patterns, K is the Scherer constant, t is the crystallite size, λ is the wavelength of x-ray, ε is the lattice strain, θ is the Bragg angle, and f is a defined function (Ref 24). Then, $B\cos\theta$ is plotted against $\sin\theta$, and using a linear extrapolation, the intercept and slope give the crystallite size and the lattice microstrain, respectively. Here, the three intense diffraction peaks corresponding to (10-10), (0001) and (10-11) planes are considered for the evaluation. Based on this method, the crystallite size of the materials after two passes of CGP is estimated to be 0.618 μm, which is basically identical with the TEM observation in Fig. 2(d) and again confirms the achieved UFG structure in the AZ31 magnesium alloy sheets.

3.2 Warm Tensile Behavior of the AZ31 Magnesium Alloy Sheets Processed by CGP

Figure 4 shows the typical engineering stress–strain curves of AZ31 magnesium alloy sheets processed by two passes of CGP tested under different deformation conditions. The variations of tensile properties with deformation temperature and strain rate are correspondingly presented in Fig. 5. In this experiment, the yield strength, tensile strength and elongation to failure of the as-annealed materials are 135.3 MPa, 234.8 MPa and 20.1%, respectively, that are tested at RT and 1×10^{-3} s^{-1} and also given in Fig. 4(c) and 5(c) for a better visualization and comparison. After two passes of CGP at 473 K, the yield strength and tensile strength of the alloy sheets are increased to 163.6 MPa and 244.9 MPa, respectively, while the elongation to failure is reduced to 11.5%, as shown in Fig. 5(c). Actually, these variations of tensile properties are very common for magnesium alloys after SPD and usually result from the synthetic action of work hardening, grain refinement and texture modification (Ref 32, 43). It should be noted that compared with the results in our previous investigation, the lower strength of the alloy sheets both before and after CGP tested in this work may be caused by the different gage orientation of tensile specimens with RD of the sheet sample, owing to its anisotropy of tensile properties and the appearance of micro-cracks at its surface (Ref 32, 33).

Obviously, the tensile deformation behavior of the materials after SPD induced by CGP is significantly influenced by deformation temperature and strain rate. When deformed at RT, the tensile properties of AZ31 magnesium alloy sheets processed by CGP show no obvious change with strain rate. With the increase in deformation temperature or the decrease in strain rate, the yield strength and tensile strength gradually decrease, while the elongation to failure exhibits an increasing trend. It has been well known that magnesium and its alloys have a poor RT formability and workability due to their HCP crystal structure and limited number of slip systems. By increasing temperature, the ductility can be improved based on the activation of additional slip systems and occurrence of DRX nearby grain or twin boundaries (Ref 44, 45). Usually, a superplastic behavior can be induced by GBS in UFG materials at elevated temperatures, which depends on the creep rate, stress, temperature and grain size (Ref 46). Thus, the grain refinement caused by SPD during CGP is expected to promote the GBS mechanism and enhance the ductility of the materials at elevated temperatures (Ref 47). However, as shown in Fig. 5, the maximum elongation to failure of only 38.7% is achieved for the specimens pulled at 1×10^{-4} s^{-1} and 473 K, and this

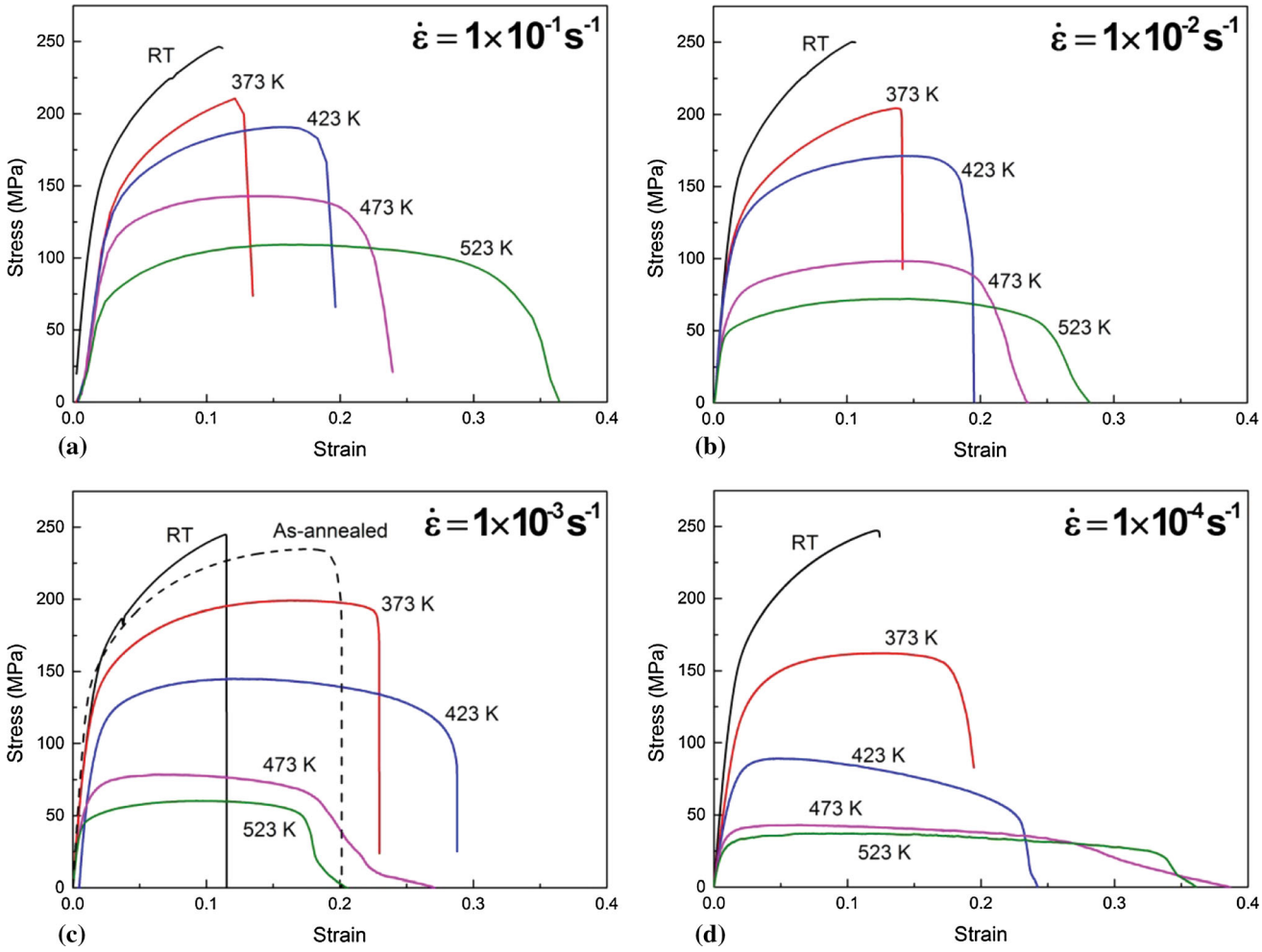

Fig. 4 Engineering stress–strain curves of AZ31 magnesium alloy sheets after CGP tested at different temperatures and strain rates of (a) 1×10^{-1} s^{-1}, (b) 1×10^{-2} s^{-1}, (c) 1×10^{-3} s^{-1} and (d) 1×10^{-4} s^{-1}. Note: The dashed line represents the curve of the as-annealed sheets before CGP

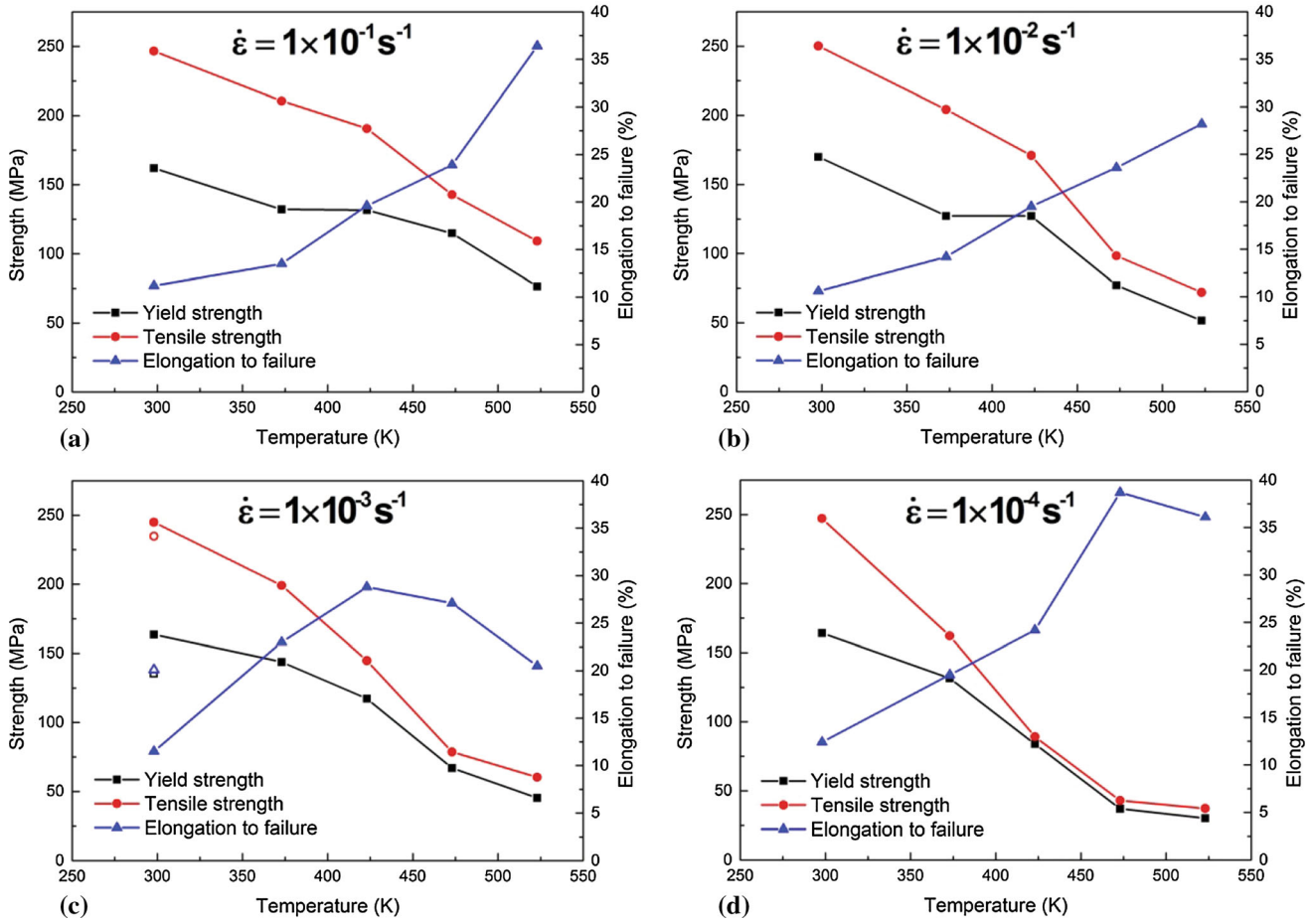

Fig. 5 Tensile properties of AZ31 magnesium alloy sheets after CGP tested at different temperatures and strain rates of (a) 1×10^{-1} s^{-1}, (b) 1×10^{-2} s^{-1}, (c) 1×10^{-3} s^{-1} and (d) 1×10^{-4} s^{-1}. Note: The hollow symbols represent the properties of the as-annealed sheets before CGP

limited ductility may suggest the negligible impact of GBS. In this situation, the yield strength and tensile strength are 37.0 MPa and 43.0 MPa, respectively. Thus, the softening behavior with increasing temperature, as observed in Fig. 4 and 5, may result from the occurrence of DRX and subsequent grain growth (Ref 48, 49). The plastic deformation of AZ31 magnesium alloys below 423 K is basically dominated by twinning and limited dislocation slip (Ref 44). At higher temperatures, the twinning becomes less, while the non-basal slip and DRX are enhanced. This enhancement is commonly seen at low strain rates. Meanwhile, the work hardening is restricted and the coarsening of new DRX grains becomes considerable with decreasing the strain rate or increasing the temperature (Ref 50). Thus, it can also be found in Fig. 5 that the decrease in yield strength and tensile strength of the materials with increasing temperature is more remarkable at a lower strain rate. Similar results were reported by Eftekhari et al. in their research on hot tensile deformation behavior of AZ31 magnesium alloy tubes processed by SPD (Ref 51). In addition, at lower strain rates of 1×10^{-4} s^{-1} and 1×10^{-3} s^{-1}, the decrease in elongation to failure at higher temperatures of 473 K and 523 K is observed. This may also be interpreted by the promoted grain coarsening at elevated temperatures and lower strain rates (Ref 52).

Usually, static toughness reflects the comprehensive mechanical properties of materials and demonstrates a combination of strength and plasticity (Ref 53, 54). The static toughness (U) can be calculated by:

$$U = \int_0^{\varepsilon_f} \sigma \mathrm{d}\varepsilon \qquad \text{(Eq 2)}$$

where σ is the flow stress and ε_f is the total strain at fracture. Since the static toughness is rarely discussed in previous research on mechanical properties of the materials after CGP, Fig. 6(a) gives the static toughness of the AZ31 magnesium alloy sheets processed by CGP tested under different deformation conditions. As seen, the static toughness of about 20 MJ/m^3 at RT is almost not affected by the strain rate. At elevated temperatures, the change of static toughness against deformation temperature varies at different strain rates. For example, at 1×10^{-4} s^{-1} and 1×10^{-3} s^{-1}, the static toughness reaches its maximum values at 373 K and, afterward, decreases noticeably with increasing temperature. This decrease is mainly attributed to the significant reduction of strength with temperature, as shown in Fig. 5(c) and (d). When the strain rate increases, the variation trend of static toughness with deformation temperature gradually changes, and its maximum value is obtained at a higher temperature than 373 K. Thus, at 1×10^{-2} s^{-1} and 1×10^{-1} s^{-1}, the evolution of static toughness may be dominated by the dramatic increase in elongation to failure as well as the relatively slow decrease in strength, as depicted in Fig. 5(a) and (b). As observed from

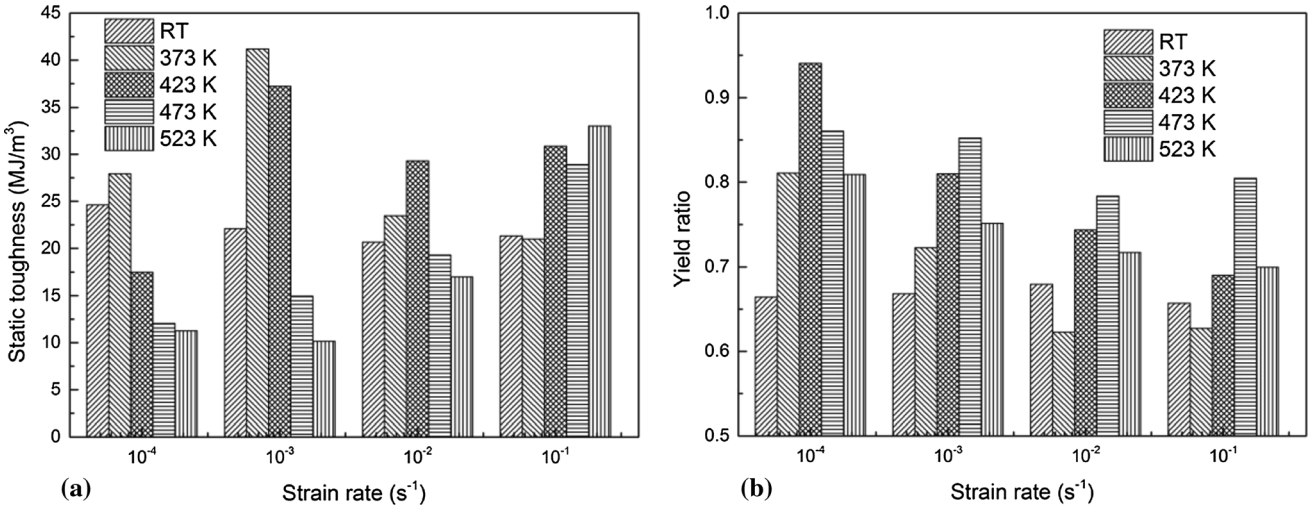

Fig. 6 (a) Static toughness and (b) yield ratio of AZ31 magnesium alloy sheets after CGP tested under different deformation conditions

Fig. 6(a), the maximum static toughness of about 41.19 MJ/m^3 is achieved at 1×10^{-3} s^{-1} and 373 K. Coincidentally, this value is almost equal to that of the as-annealed sheets before CGP tested at 1×10^{-3} s^{-1} and RT, which is about 41.22 MJ/m^3.

It is worth noting from Fig. 5 that the difference between the yield strength and the tensile strength gradually decreases with the increase in deformation temperature or the decrease in strain rate. To further explore this phenomenon, the yield ratio representing the ratio of yield strength to tensile strength of the materials is calculated and presented in Fig. 6(b). As known, during a tensile test, the tensile strength corresponds to the plastic instability point of the materials. The yield ratio is an evaluation of strain hardening potential, and generally a low yield ratio indicates a large strain hardening potential (Ref 55, 56). As shown in Fig. 6(b), at elevated temperatures, the level of yield ratio roughly decreases as the strain rate increases, suggesting an enhanced strain hardening ability. However, at a given strain rate, the strain hardening ability firstly decreases and then increases with increasing temperature, just opposite to the variation of yield ratio. Generally, the strain hardening exponent (n) is utilized to evaluate the uniform deformation capability of the materials, and it can be calculated as the slope of $\ln\sigma - \ln\varepsilon$ plot for the uniform plastic deformation region of the stress–strain curve under given deformation conditions (Ref 52).

$$n = \left.\frac{\partial \ln \sigma}{\partial \ln \varepsilon}\right|_{\dot{\varepsilon},T} \quad \text{(Eq 3)}$$

The variation of strain hardening exponent under different deformation conditions is shown in Fig. 7(a). Similar to the tensile properties, the value of n shows no significant change with the strain rate at RT, while it increases gradually with increasing strain rate at elevated temperatures, and its dependence on strain rate is more remarkable at lower deformation temperatures. Meanwhile, for a given strain rate, the strain hardening exponent shows a decreasing trend with increasing temperature.

Generally, there are four distinct stages during tensile deformation of most alloys and metals consisted of uniform deformation, diffuse necking, localized necking and final fracture (Ref 52, 57). As demonstrated by the engineering stress–strain curves in Fig. 4, when tested at RT and 373 K, the flow stress rises to the peak value due to strain hardening and decreases rapidly until fracture with very limited necking stage (Ref 30). At elevated temperatures, after reaching the peak value, the flow stress decreases more gradually until failure and distinct necking occurs. The above mentioned decrease in strain hardening ability with decreasing strain rate is resulted from the softening effect due to the operation of accelerated dynamic recovery as the main restoration process at elevated temperatures, which sufficiently balances the rate of strain hardening (Ref 30, 58). And such recovery-controlled steady state flow is usually observed at relatively low strain rates. It is known that the appearance of peak stress is a typical characteristic of DRX, usually causing the formation of fine grains (Ref 58). Thus, in this investigation, the occurrence of DRX softening at elevated temperatures also contributes to the decrease in the strain amount to the peak stress (Ref 52). Moreover, the lowest level of strain hardening exponent is obtained at 473 K, and then experiences a recovery when the deformation temperature increases to 523 K, which will be explained by the microstructural evolution discussed in the following section.

The strain hardening exponent is very low (0.10-0.15) at high temperatures or low strain rates and, after reaching the tensile strength, the engineering stress–strain curves exhibit a distinct necking stage, as shown in Fig. 4. Usually, the strain rate sensitivity coefficient (m) reflects the transfer and diffusion ability of necking, and it can be evaluated by the slope of $\ln\sigma - \ln\dot{\varepsilon}$ plot.

$$m = \left.\frac{\partial \ln \sigma}{\partial \ln \dot{\varepsilon}}\right|_{\varepsilon,T} \quad \text{(Eq 4)}$$

Accordingly, the line fitting method is used, and the values of m are achieved as the slope of each plot, as presented in Fig. 7(b). Here, a fixed strain of 0.1 within the uniform plastic deformation region is selected for the calculation. In general, a higher m value promotes the necking resistance, leading to a higher elongation to failure (Ref 59). Obviously, the value of m gradually increases with increasing temperature, and the higher values of ~ 0.17 and ~ 0.14 are obtained at 473 K and 523 K, respectively. Unfortunately, the m values obtained in this study

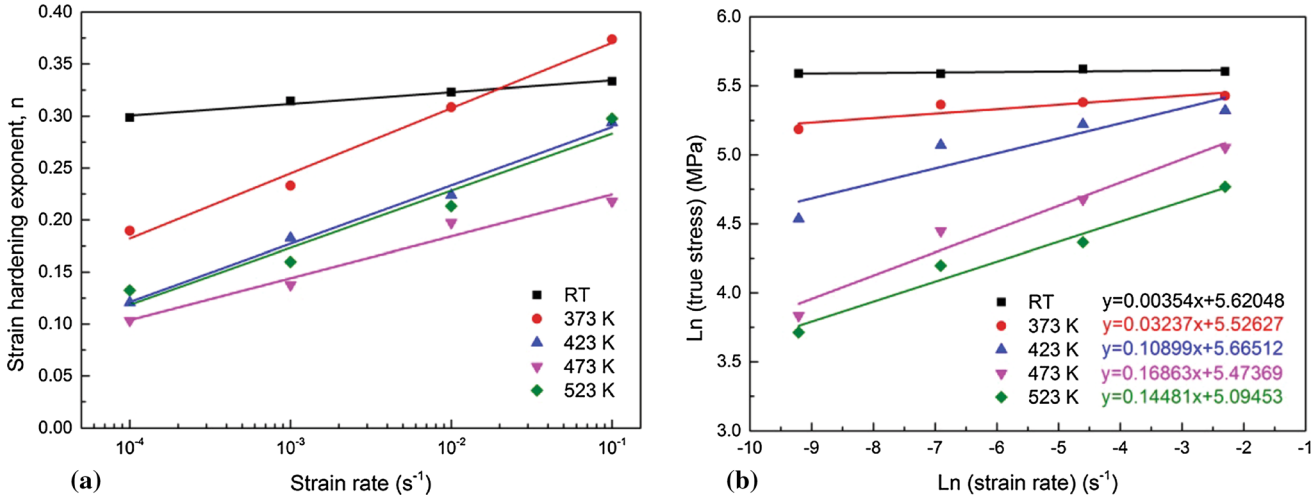

Fig. 7 Variations of (a) strain hardening exponent (n) and (b) strain rate sensitivity coefficient (m) of the CGP sheets under different deformation conditions

are lower than that required for superplasticity ($m > 0.30$). It is believed that grain size and deformation temperature are the two important factors for achieving superplastic behavior (Ref 51). Thus, despite the refinement of average grain size to around 3.2 μm for the materials after two passes of CGP, as shown in Fig. 2(c), the preserved bimodal structure may account for the limited ductility and the absence of superplasticity. In addition, the temperature range for tensile tests is relatively low in this experiment, which may also not favor the achievement of superplasticity (Ref 60).

Evidently, the tensile behavior of AZ31 magnesium alloy sheets processed by CGP is significantly influenced by deformation conditions. In order to clearly analyze the effect of deformation temperature/strain rate on the microstructural evolution and the fracture morphology of tensile specimens and further explore the deformation mechanism, a fixed value of strain rate/deformation temperature should be selected. Grain refinement induced by DRX may be less effective at higher temperatures due to rapid grain growth. As anticipated, the highest deformation temperature of 523 K adopted in this experiment is relatively low, and it may not favor the grain growth, but benefit from the positive effect of DRX. From this point of view, DRX may be interrupted at higher strain rates before its completion since the specimens may fracture at lower elongation to failure. Thus, combined with the analysis based on Fig. 4, 5, 6, 7, it is believed that the results at strain rate of 1×10^{-4} s^{-1} or at temperature of 523 K should be the most representative to reveal the effects of deformation conditions on the microstructural evolution and fracture morphology of tensile specimens, which will be discussed in the following sections.

3.3 Effects of Deformation Conditions on Microstructural Evolution

Figure 8 shows the optical micrographs in gage region and gripper region of tensile specimens tested at different deformation temperatures and strain rate of 1×10^{-4} s^{-1}. To be pointed out, the microstructural evolution in the gripper region is only induced by static annealing without any straining. Obviously, at RT and 373 K, the bimodal structure similar to that of the materials processed after CGP still exists in the gripper region, as shown in Fig. 8b and d. As the temperature increases, grain growth happens and the fine DRX grains initially formed at the grain/twin boundaries during CGP gradually disappear, as manifested in Fig. 8f, h and j. The average grain sizes are increased to 11.6 μm and 16.5 μm at 473 K and 523 K, respectively. In contrast, the microstructural evolution in the gage region is significantly influenced by the deformation temperature. As shown in Fig. 8a and c, when tested at RT and 373 K, numerous deformation twins are observed in the microstructure to coordinate the plastic deformation owing to the limited formability of the materials at these low temperatures. This may interpret the sudden decrease in flow stress after the peak value and the low strain rate sensitivity coefficient under these conditions, as mentioned above. When the temperature is increased to 423 K, more fine grains are generated due to partial DRX, causing the remarkable softening effect and gradual decrease of flow stress, as shown in Fig. 4(d) (Ref 30). Meanwhile, no twins are found in the microstructure shown in Fig. 8(e), and the fine grains form at the boundaries of the initial large grains (Ref 61). At a higher temperature of 473 K, the DRX process is promoted and the microstructure is further refined despite that there are still some coarse grains, as shown in Fig. 8(g). Then, as seen in Fig. 8(i), the grain growth is more significant at 523 K, and the average grain size is about 9.6 μm which is comparable to that without tensile deformation (Fig. 8j). This grain coarsening may result in the slight decrease in elongation to failure and strain rate sensitivity coefficient, and the recovery of strain hardening exponent at 523 K, as demonstrated in Fig. 5 and 7.

Figure 9 shows the optical micrographs in gage region and gripper region of tensile specimens tested at 523 K and different strain rates. Actually, the effect of strain rate on microstructural evolution in the gripper region is basically resulted from different static annealing time. As shown in Fig. 9(b), despite the limited annealing time at the strain rate of 1×10^{-1} s^{-1}, the bimodal structure formed during CGP has disappeared. Then, with decreasing strain rate or increasing annealing time, the microstructure in the gripper region experiences negligible grain coarsening, as shown in Fig. 9(d), (f) and (h). However, the influence of strain rate on microstructure in the gage region is more significant. When deformed at

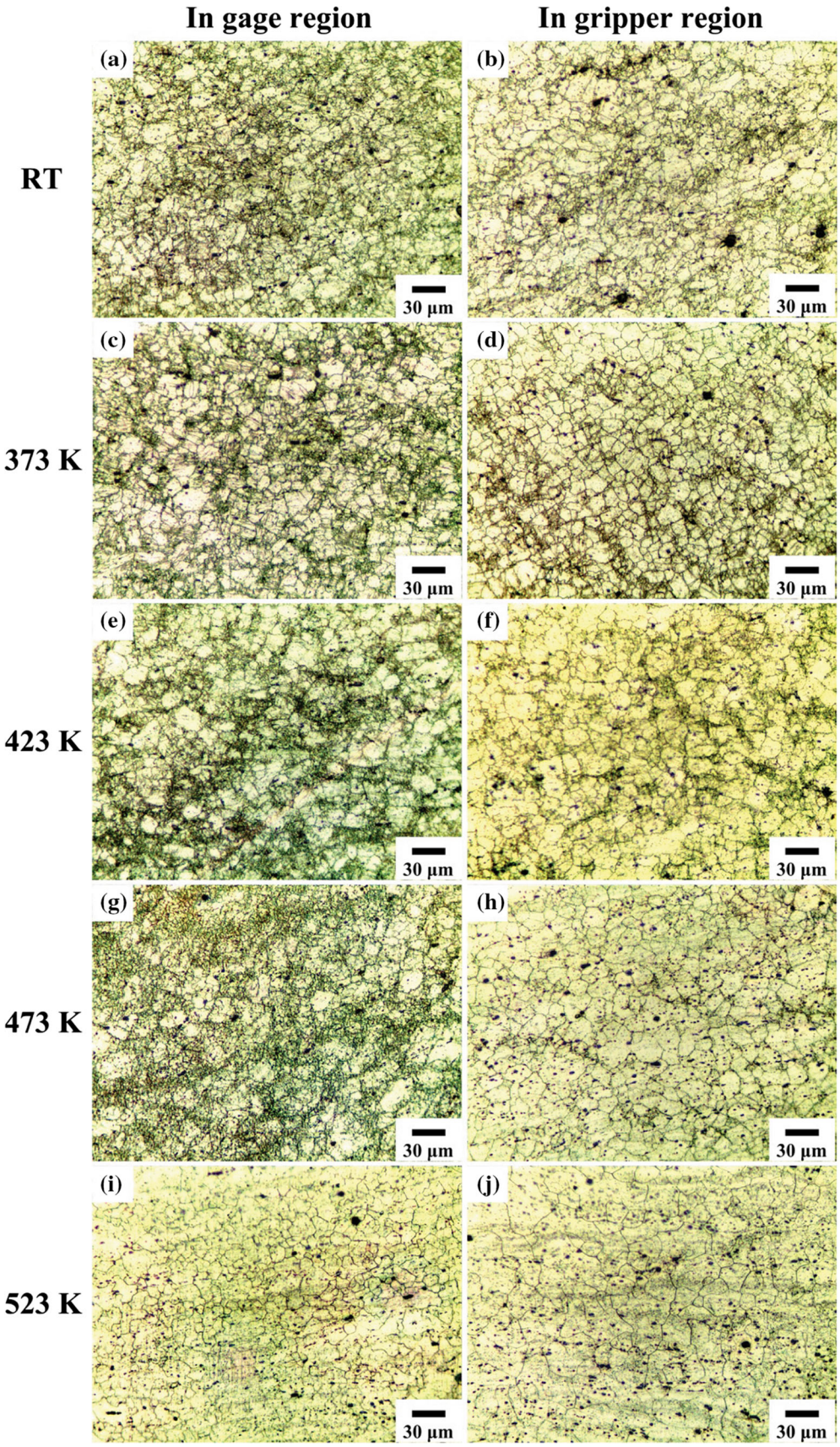

Fig. 8 Optical micrographs in different regions of tensile specimens tested at different deformation temperatures and strain rate of 1×10^{-4} s^{-1}: In (a) gage and (b) gripper regions at RT, in (c) gage and (d) gripper regions at 373 K, in (e) gage and (f) gripper regions at 423 K, in (g) gage and (h) gripper regions at 473 K and in (i) gage and (j) gripper regions at 523 K

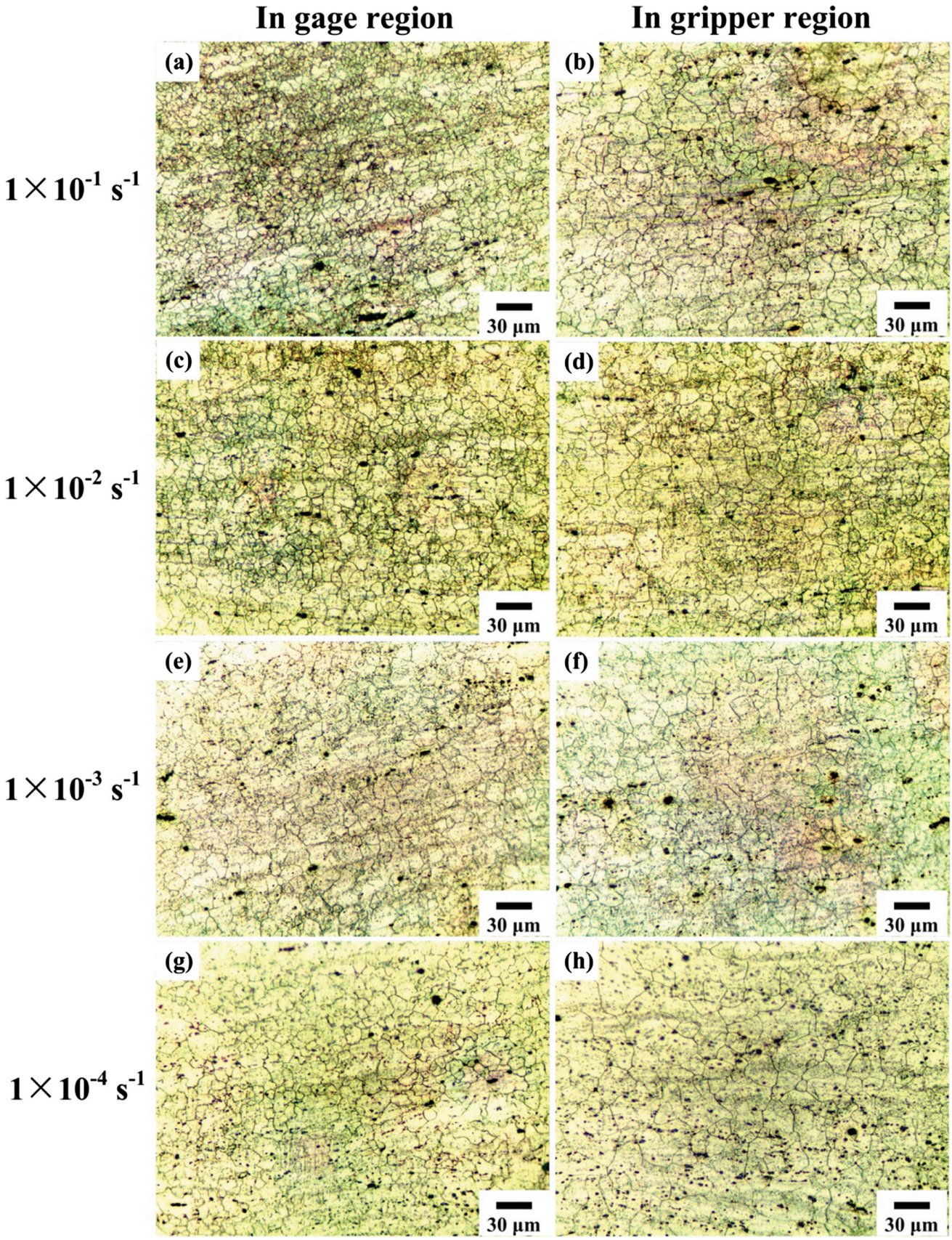

Fig. 9 Optical micrographs in different regions of tensile specimens tested at 523 K and different strain rates: In (a) gage and (b) gripper regions at 1×10^{-1} s^{-1}, in (c) gage and (d) gripper regions at 1×10^{-2} s^{-1}, in (e) gage and (f) gripper regions at 1×10^{-3} s^{-1} and in (g) gage and (h) gripper regions at 1×10^{-4} s^{-1}

523 K, grain refinement due to DRX and subsequent grain growth occur successively. The nucleation and growth of DRX grains are sensitive to strain rate, so the coupled effect of strain rate and deformation temperature may play a key role in microstructural evolution in the gage region (Ref 52). As can be seen in Fig. 9(a), partial DRX occurs at the strain rate of 1×10^{-1} s^{-1}, and relatively refined grains with the average size of around 5.4 μm are achieved. However, no further grain refinement is observed with decreasing strain rate, while the grain coarsening is gradually promoted due to the longer deformation time, as shown in Fig. 9c, e and g, and the softening effect observed in Fig. 4 and 5 is enhanced.

3.4 Fracture Morphology Analysis

Figure 10 shows the fracture morphology of tensile specimens tested at different temperatures and strain rate of 1×10^{-4} s^{-1}. Obviously at RT, the macroscopic fracture surface shows no obvious shrinkage (Fig. 10a), which confirms the absence of necking stage and the sudden rupture beyond tensile strength of the engineering stress–strain curve, as shown in Fig. 4d. Meanwhile, there are lots of typical cleavage facets, while dimples can hardly be seen at the fracture surface, suggesting a brittle fracture mode. At 373 K, limited shrinkage of the macroscopic fracture surface is evident in Fig. 10b, and dimples begin to appear at the fracture surface. This means that the specimen experiences a certain degree of diffusion necking before failure, and the fracture mode transforms to be a combination of ductile fracture and brittle fracture. This is very common to deformation by twinning in magnesium alloys with moderate ductility at low temperatures, which is verified by the microstructural observation in Fig. 8a and c (Ref 62). Then, as the deformation temperature increases, the fracture surfaces are gradually occupied by dimples, indicating the nucleation, growth and coalescence of the voids (Ref 63). As shown in Fig. 10c, a cone-shape localized necking area with many micro-voids is observed at the macroscopic fracture surface (Ref 52). Lots of dimples with different sizes and depths appear at the fracture surface, which may be related to the initial bimodal structure despite the occurrence of DRX. Together with numerous tearing edges, a typical ductile fracture characteristic is revealed at 423 K accompanied by a considerable diffusion necking stage of the specimen. When the temperature increases to 473 K, a larger number of dimples are found to be more shallow, owing to the further grain refinement introduced by DRX (Fig. 10d). Thus, as demonstrated in Fig. 7b, the highest m value is achieved under this condition, which is related to an enhanced capacity of the diffuse necking as well as the extended elongation to failure. At 523 K, as shown in Fig. 10e, the dimples become larger and deeper, compared with those at 473 K, due to grain coarsening at this higher temperature (Ref 64). Meantime, the rapid growth of the DRX grains results in the distinct localized necking at the macroscopic fracture surface. It can be concluded that the ductile fracture mode is dominant at elevated temperatures from 423 K to 523 K, and the fracture morphology agrees very well with the microstructural evolution, as shown in Fig. 8.

Figure 11 shows the fracture morphology of tensile specimens tested at 523 K and different strain rates. Evidently, all the specimens have a cone-shape localized necking area at this temperature, and the specimen pulled at the strain rate of 1×10^{-1} s^{-1} has the most localized necking area at the microscopic fracture surface, as shown in Fig. 11a. Meanwhile, a large number of dimples with various sizes and depths as well as lots of sharp tearing edges are observed, demonstrating the typical characteristic of ductile fracture mode at this strain rate. Additionally, as can be seen in Fig. 11a and b, there are some small dimples distributing at the bottom of big dimples at higher strain rates of 1×10^{-1} s^{-1} and 1×10^{-2} s^{-1}. In these situations, when the small dimples extend to a certain size, a large stress concentration will be caused and the materials between adjacent dimples will be torn off, forming the blade type edges. Besides, some second-phase particles are also observed at the bottom of the big dimples, which are thought to be the nucleation center of voids under these deformation conditions (Ref 65). It has been reported by Deng. et al. that the void coalescence and the intergranular fracture are the two main fracture mechanisms (Ref 52). Usually at a higher strain rate, the void coalescence plays a more important role during the fracture of the specimens because the grains have not enough time to grow (Ref 66). In this investigation, with the decrease in strain rate, only the number of dimples is gradually reduced, and the dimples become larger and deeper, as shown in Fig. 11c and d. With decreasing strain rate, the voids nucleating at grain boundaries will have sufficient time to facilitate subsequent coalescence and growth in size (Ref 30). This also means that the predominately ductile fracture occurs at all strain rates and 523 K, and the void coalescence is the dominant fracture mechanism under these conditions. Additionally, the absence of intergranular fracture may suggest negligible contribution of GBS to the tensile deformation.

In order to further explore the deformation mechanism of the AZ31 magnesium alloy sheets processed by CGP, the apparent activation energy (Q) of the materials are adopted and evaluated under the given strain of 0.1 by:

$$Q = RN \frac{\partial \ln \sigma}{\partial \frac{1}{T}} \quad \text{(Eq 5)}$$

where σ is the flow stress, N is the stress exponent ($N = 1/m$), R is the universal gas constant, and T is the deformation temperature (Ref 30). Figure 12 presents the plot curves of $\ln \sigma - 1000/T$ under different deformation conditions. Obviously, the apparent activation energy shows a great dependence on deformation temperature and strain rate and, basically, with increasing temperature or decreasing strain rate, the Q value increases gradually. According to Eq. 5, the values of apparent activation energy are estimated from the slopes of the plot curves in Fig. 12. The Q values at 423-523 K and strain rates of 1×10^{-4}-1×10^{-1} s^{-1} are calculated to be 68.8-105.5 kJ/mol, which covers the grain boundary diffusion activation energy (92 kJ/mol) and lower than the lattice self-diffusion activation energy of magnesium (135 kJ/mol) (Ref 67). Accordingly, the tensile deformation of the materials may be predominately controlled by grain boundary diffusion associated with GBS, DRX and grain growth processes (Ref 68-70).

Fong et al. previously attributed the absence of superplasticity to the low thermal stability of the fine grains at elevated temperatures due to the large stored strain energy and driving force for grain growth (Ref 30). In their work, a directly orthogonal CGP procedure including four successive groove pressings with a 90° rotation around ND of the sheet sample after each pressing and a final flattening was adopted (Ref 28). The AZ31 magnesium alloy sheets experienced complex plastic deformation and very large straining, and the microstructure

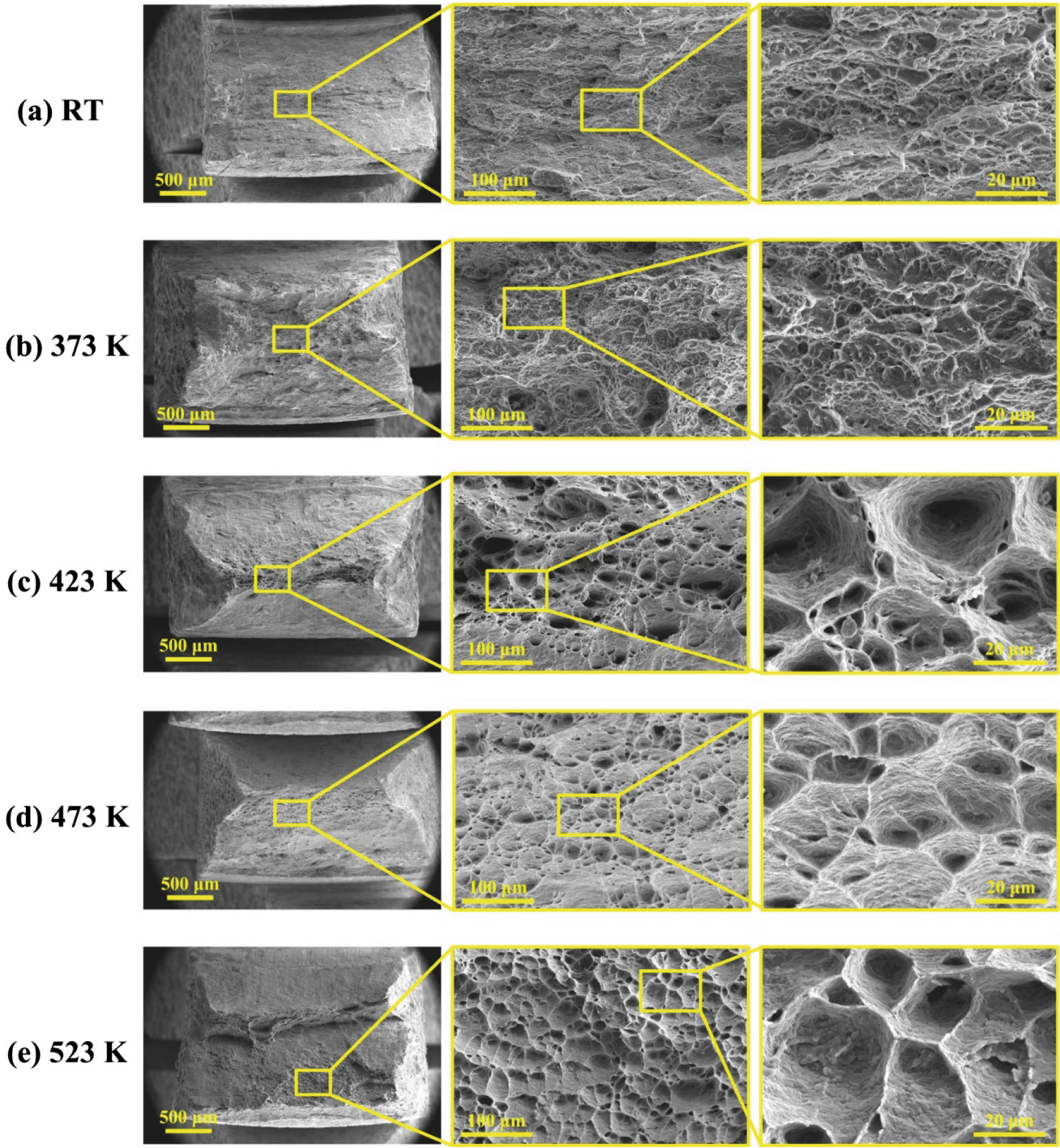

Fig. 10 Fracture morphology of tensile specimens tested at (a) RT, (b) 373 K, (c) 423 K, (d) 473 K and (e) 523 K and strain rate of 1×10^{-4} s^{-1}

exhibited low thermal stability. In this investigation, two passes of traditional CGP procedure as well as an effective strain of about 2.32 was introduced to the alloy sheets, as illustrated in Fig. 1. The UFG structure is finally achieved and also has a relatively low thermal stability, similar to that obtained by Fong et al. [28, 30). More importantly, only partial DRX happens in the materials processed by two passes of CGP at a relatively low temperature of 473 K and the bimodal structure consisted of initial coarse grains and new fine DRX grains are developed and preserved eventually as the initial microstructure of the alloy sheets subjected to the subsequent tensile tests under different conditions. Although substructured/deformed (sub)-grains may form in the initial coarse grains, the bimodal structure and the relatively low temperatures for the tensile tests still cannot promote the GBS mechanism. Thus, given the absence of superplasticity suggested by the limited ductility and the relatively low *m* values, DRX and grain growth should be the dominant mechanism accounting for the warm tensile deformation of AZ31 magnesium alloy sheets processed by CGP, while GBS mechanism may contribute very little to their

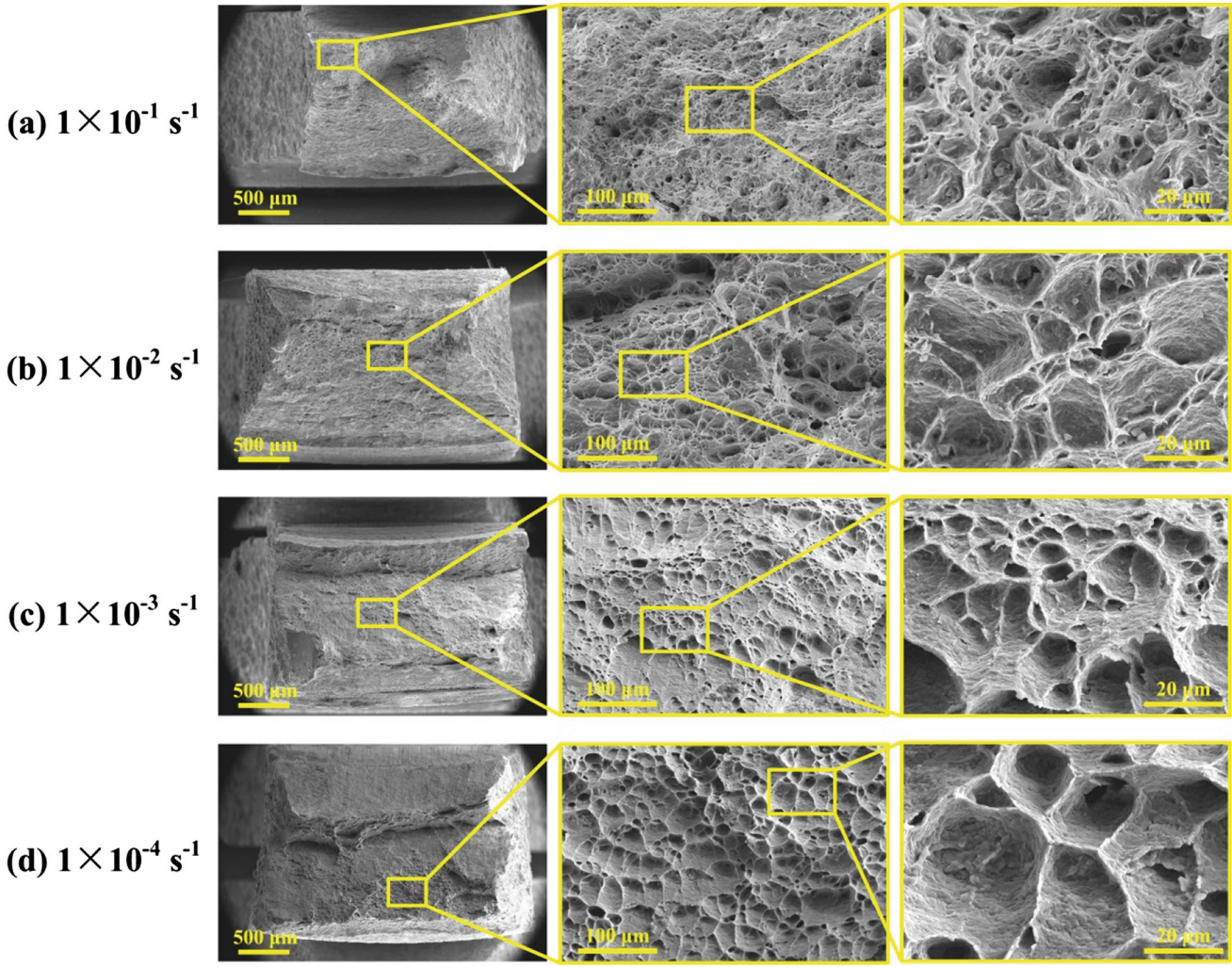

Fig. 11 Fracture morphology of tensile specimens tested at 523 K and strain rates of (a) 1×10^{-1} s^{-1}, (b) 1×10^{-2} s^{-1}, (c) 1×10^{-3} s^{-1} and (d) 1×10^{-4} s^{-1}

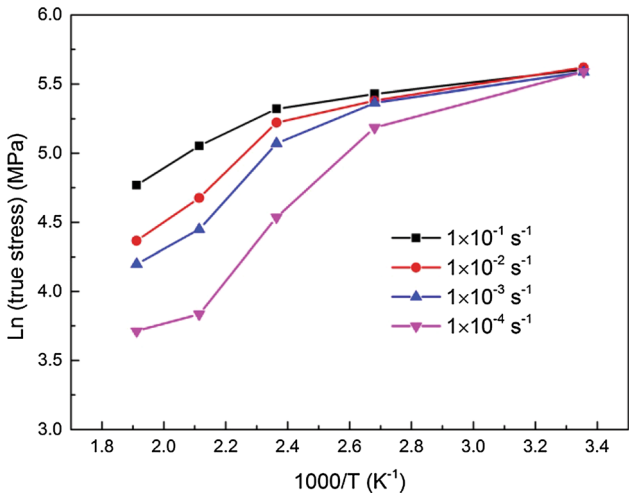

Fig. 12 Variation of activation energy curves of the CGP sheets under different deformation conditions

deformation behavior under the conditions investigated in this work (Ref 48, 71).

4. Conclusions

In the present work, the as-annealed AZ31 magnesium alloy sheets were processed by two passes of CGP at 473 K, and then the warm tensile deformation and fracture behavior of the processed materials at different deformation temperatures and strain rates were investigated. The most important conclusions are summarized as follows:

(1) Coarse and equiaxed grains with the average size of about 11.3 μm are obtained in the as-annealed AZ31 magnesium alloy sheets, and UFG structure is achieved in the materials after two passes of CGP at 473 K. Sub-grains of about 0.5 μm are observed in TEM micrograph, which is also confirmed by XRD analysis. A bimodal structure is developed due to partial DRX and deformation homogeneity.

(2) The tensile flow behavior of the alloy sheets processed by CGP is significantly influenced by deformation tem-

perature and strain rate. With increasing temperature or decreasing strain rate, the yield strength and tensile strength gradually decrease, while the elongation to failure shows an increasing trend. The maximum elongation to failure of 38.7% is achieved at 1×10^{-4} s^{-1} and 473 K, and the yield strength and tensile strength are 37.0 MPa and 43.0 MPa, respectively. The maximum static toughness of about 41.19 MJ/m^3 is achieved at 1×10^{-3} s^{-1} and 373 K, which is comparable to about 41.22 MJ/m^3 of the as-annealed sheets tested at 1×10^{-3} s^{-1} and RT.

(3) Both the yield ratio and strain hardening exponent demonstrate that the strain hardening ability of the processed alloy sheets shows no obvious change with strain rate at RT while, at elevated temperatures, it increases gradually with increasing strain rate, and its dependence on strain rate is more significant at lower temperatures. For a given strain rate, the lowest level of strain hardening exponent is obtain at not 523 K, but 473 K, which is related to the grain growth at 523 K.

(4) The microstructural evolution in the gage region is greatly affected by deformation temperature and strain rate. At RT and 373 K, lots of twins are found to coordinate plastic deformation. With increasing temperature, grain refinement caused by DRX is observed at 423 K and 473 K, and obvious grain coarsening happens at 523 K. With decreasing strain rate, the grain coarsening is gradually promoted owing to the longer deformation time at 523 K.

(5) The fracture morphology shows that with increasing temperature, the fracture mode changes from brittle fracture to ductile fracture. At 523 K, as the strain rate decreases, the number of dimples is gradually reduced and the dimples become larger and deeper, demonstrating the ductile fracture mode dominated by void coalescence. The fracture morphology is closely related to the microstructural evolution of the materials under different deformation conditions.

(6) The strain rate sensitivity coefficient gradually increases with increasing temperature, and the relatively high values of ~ 0.17 and ~ 0.14 are obtained at 473 K and 523 K, respectively. The apparent activation energy at 423-523 K is estimated to be 68.8-105.5 kJ/mol, which covers the grain boundary diffusion activation energy and lower than the lattice self-diffusion activation energy of magnesium. Considering the limited ductility and the relatively low m values demonstrating the absence of superplasticity, DRX and grain growth should be the dominant mechanism accounting for the warm tensile deformation of AZ31 magnesium alloy sheets processed by CGP, while GBS mechanism may contribute little, due to the initial bimodal structure and the relatively low temperatures for the tensile tests in this experiment.

Acknowledgments

The authors would like to acknowledge the financial support provided by National Natural Science Foundation of China (Grant No. 51605266), Shandong Provincial Natural Science Foundation (Grant No. ZR2018QEM001) and Natural Science Foundation of Jiangsu Province (Grant No. BK20180231).

Conflict of interest

The authors declare that they have no known conflict of interest or personal relationships that could have appeared to influence the work reported in this paper.

References

1. A. Fata, G. Faraji, M.M. Mashhadi, and V. Tavakkoli, Hot Tensile Deformation and Fracture Behavior of Ultrafine-Grained AZ31 Magnesium Alloy Processed by Severe Plastic Deformation, *Mater. Sci. Eng. A*, 2016, **674**, p 9–17
2. J. Jia, Y. Xu, Y. Yang, C. Chen, W. Liu, L. Hu, and J. Luo, Microstructure Evolution of an AZ91D Magnesium Alloy Subjected to Intense Plastic Straining, *J. Alloy. Compd.*, 2017, **721**, p 347–362
3. G. Song and A. Atrens, Understanding Magnesium Corrosion-A Framework for Improved Alloy Performance, *Adv. Eng. Mater.*, 2003, **5**, p 837–858
4. A. Atrens, G. Song, F. Cao, Z. Shi, and P.K. Bowen, Advances in Mg Corrosion and Research Suggestions, *J. Magnes. Alloy.*, 2013, **1**, p 177–200
5. C. Liu, Q. Li, J. Liang, J. Zhou, and L. Wang, Microstructure and Corrosion Behaviour of Laser Surface Melting Treated WE43 Magnesium Alloy, *RSC Adv.*, 2016, **6**, p 30642–30651
6. R.Z. Valiev, R.K. Islamgaliev, and I.V. Alexandrov, Bulk Nanostructured Materials from Severe Plastic Deformation, *Prog. Mater Sci.*, 2000, **45**, p 103–189
7. R.Z. Valiev, Y. Estrin, Z. Horita, T.G. Langdon, M.J. Zechetbauer, and Y.T. Zhu, Producing Bulk Ultrafine-Grained Materials by Severe Plastic Deformation, *JOM-US*, 2006, **58**, p 33–39
8. C.P. Wang, F.G. Li, L. Wang, and H.J. Qiao, Review on Modified and Novel Techniques of Severe Plastic Deformation, *Sci. China Technol. Sc.*, 2012, **55**, p 2377–2390
9. R.Z. Valiev and T.G. Langdon, Principles of Equal-Channel Angular Pressing as a Processing Tool for Grain Refinement, *Prog. Mater Sci.*, 2006, **51**, p 881–981
10. A.P. Zhilyaev and T.G. Langdon, Using High-pressure Torsion for Metal Processing: Fundamentals and Applications, *Prog. Mater Sci.*, 2008, **53**, p 893–979
11. Y. Saito, H. Utsunomiya, N. Tsuji, and T. Sakai, Novel Ultra-high Straining Process for Bulk Materials-Development of the Accumulative Roll-Bonding (ARB) Process, *Acta Mater.*, 1999, **47**, p 579–583
12. N. Tsuji, Y. Saito, S. Lee, and Y. Minamino, ARB (Accumulative Roll-Bonding) and Other New Techniques to Produce Bulk Ultrafine Grained Materials, *Adv. Eng. Mater.*, 2003, **5**, p 338–344
13. A. Azushima, R. Kopp, A. Korhonen, D.Y. Yang, F. Micari, G.D. Lahoti, P. Groche, J. Yanagimoto, N. Tsuji, A. Rosochowski, and A. Yanagida, Severe Plastic Deformation (SPD) Processes for Metals, *CIRP Ann. Manuf. Techn.*, 2008, **57**, p 716–735
14. D.H. Shin, J. Park, Y. Kim, and K. Park, Constrained Groove Pressing and its Application to Grain Refinement of Aluminum, *Mater. Sci. Eng. A*, 2002, **328**, p 98–103
15. A.K. Gupta, T.S. Maddukuri, and S.K. Singh, Constrained Groove Pressing for Sheet Metal Processing, *Prog. Mater Sci.*, 2016, **84**, p 403–462
16. A. Krishnaiah, U. Chakkingal, and P. Venugopal, Production of Ultrafine Grain Sizes in Aluminium Sheets by Severe Plastic Deformation Using the Technique of Groove Pressing, *Scripta Mater.*, 2005, **52**, p 1229–1233
17. J. Zrnik, T. Kovarik, Z. Novy, and M. Cieslar, Ultrafine-Grained Structure Development and Deformation Behavior of Aluminium Processed by Constrained Groove Pressing, *Mater. Sci. Eng. A*, 2009, **503**, p 126–129
18. H. Pouraliakbar, M.R. Jandaghi, S.J.M. Baygi, and G. Khalaj, Microanalysis of Crystallographic Characteristics and Structural Transformations in SPDed Al-Mn-Si Alloy by Dual-Straining, *J. Alloy. Compd.*, 2017, **696**, p 1189–1198
19. M. Moradpour, F. Khodabakhshi, and H. Eskandari, Dynamic Strain Aging Behavior of an Ultra-Fine Grained Al-Mg Alloy (AA5052)

Processed Via Classical Constrained Groove Pressing, *J. Mater. Res. Technol.*, 2019, **8**, p 630–643
20. S. Ghorbanhosseini, F. Fereshteh-Saniee, and A. Sonboli, An Experimental Investigation on the Influence of Elevated-Temperature Constrained Groove Pressing on the Microstructure, Mechanical Properties, Anisotropy and Texture of 2024 Al Sheets, *J. Alloy. Compd.*, 2020, **817**, p 152763
21. A. Krishnaiah, U. Chakkingal, and P. Venugopal, Applicability of the Groove Pressing Technique for Grain Refinement in Commercial Purity Copper, *Mater. Sci. Eng. A*, 2005, **410–411**, p 337–340
22. K. Peng, L. Su, L.L. Shaw, and K.W. Qian, Grain Refinement and Crack Prevention in Constrained Groove Pressing of Two-Phase Cu-Zn Alloys, *Scripta Mater.*, 2007, **56**, p 987–990
23. K. Peng, X. Mou, J. Zeng, L.L. Shaw, and K.W. Qian, Equivalent Strain, Microstructure and Hardness of H62 Brass Deformed by Constrained Groove Pressing, *Comp. Mater. Sci.*, 2011, **50**, p 1526–1532
24. F. Khodabakhshi, M. Kazeminezhad, and A.H. Kokabi, Constrained Groove Pressing of Low Carbon Steel: Nano-structure and Mechanical Properties, *Mater. Sci. Eng. A*, 2010, **527**, p 4043–4049
25. F. Khodabakhshi and M. Kazeminezhad, The Effect of Constrained Groove Pressing on Grain Size, Dislocation Density and Electrical Resistivity of Low Carbon Steel, *Mater. Des.*, 2011, **32**, p 3280–3286
26. F. Khodabakhshi and M. Kazeminezhad, The Annealing Phenomena and Thermal Stability of Severely Deformed Steel Sheet, *Mater. Sci. Eng. A*, 2011, **528**, p 5212–5218
27. B.R. Sunil, A.A. Kumar, T.S.S. Kumar, and U. Chakkingal, Role of Biomineralization on the Degradation of Fine Grained AZ31 Magnesium Alloy Processed by Groove Pressing, *Mater. Sci. Eng. C*, 2013, **33**, p 1607–1615
28. K.S. Fong, D. Atsushi, T.M. Jen, and B.W. Chua, Effect of Deformation and Temperature Paths in Severe Plastic Deformation Using Groove Pressing on Microstructure, Texture, and Mechanical Properties of AZ31-O, *ASME J. Manuf. Sci. Eng.*, 2015, **137**, p 051004
29. K.S. Fong, M.J. Tan, F.L. Ng, A. Danno, and B.W. Chua, Microstructure Stability of a Fine-Grained AZ31 Magnesium Alloy Processed by Constrained Groove Pressing during Isothermal Annealing, *ASME J. Manuf. Sci. Eng.*, 2017, **139**, p 081007
30. K.S. Fong, A. Danno, M.J. Tan, and B.W. Chua, Tensile Flow Behavior of AZ31 Magnesium Alloy Processed by Severe Plastic Deformation and Post-Annealing at Moderately High Temperatures, *J. Mater. Process. Technol.*, 2017, **246**, p 235–244
31. M.M. Hoseini-Athar, R. Mahmudi, R.P. Babu, and P. Hedström, Microstructural Evolution and Superplastic Behavior of a Fine-Grained Mg-Gd Alloy Processed by Constrained Groove Pressing, *Mater. Sci. Eng. A*, 2019, **754**, p 390–399
32. Z. Wang, Y. Guan, T. Wang, Q. Zhang, X. Wei, X. Fang, G. Zhu, and S. Gao, Microstructure and Mechanical Properties of AZ31 Magnesium Alloy Sheets Processed by Constrained Groove Pressing, *Mater. Sci. Eng. A*, 2019, **745**, p 450–459
33. Z. Wang, Y. Guan, G. Wang, and C. Zhong, Influences of Die Structure on Constrained Groove Pressing of Commercially Pure Ni Sheets, *J. Mater. Process. Technol.*, 2015, **215**, p 205–218
34. T. Krajňák, P. Minárik, J. Stráská, J. Gubicza, K. Máthis, and M. Janeček, Influence of Equal Channel Angular Pressing Temperature on Texture, Microstructure and Mechanical Properties of Extruded AX41 Magnesium, *J. Alloy. Compd.*, 2017, **705**, p 273–282
35. R.B. Figueiredo and T.G. Langdon, Principles of Grain Refinement in Magnesium Alloys Processed by Equal-Channel Angular Pressing, *J. Mater. Sci.*, 2009, **44**, p 4758–4762
36. R.B. Figueiredo and T.G. Langdon, Grain Refinement and Mechanical Behavior of a Magnesium Alloy Processed by ECAP, *J. Mater. Sci.*, 2010, **45**, p 4827–4836
37. Z. Wang, Y. Guan, and P. Liang, Deformation Efficiency, Homogeneity, and Electrical Resistivity of Pure Copper Processed by Constrained Groove Pressing, *Rare Met.*, 2014, **33**, p 287–292
38. P.C. Yadav, A. Sinhal, S. Sahu, A. Roy, and S. Shekhar, Microstructural Inhomogeneity in Constrained Groove Pressed Cu-Zn Alloy Sheet, *J. Mater. Eng. Perform.*, 2016, **25**, p 2604–2614
39. J. Victoria-Hernández, J. Suh, S. Yi, J. Bohlen, W. Volk, and D. Letzig, Strain-Induced Selective Grain Growth in AZ31 Mg Alloy Sheet Deformed by Equal Channel Angular Pressing, *Mater. Charact.*, 2016, **113**, p 98–107
40. T. Ungár, Microstructural Parameters from x-ray Diffraction Peak Broadening, *Scripta Mater.*, 2004, **51**, p 777–781
41. S.S.S. Kumar and T. Raghu, Structural and mechanical behaviour of severe plastically deformed high purity aluminium sheets processed by constrained groove pressing technique, *Mater. Des.*, 2014, **57**, p 114–120
42. P. Mukherjee, A. Sarkar, and P. Barat, Microstructural Changes in Oxygen-Irradiated Zirconium-Based Alloy Characterised by x-ray Diffraction Techniques, *Mater. Charact.*, 2005, **55**, p 412–417
43. T. Han, G. Huang, Q. Deng, G. Wang, B. Jiang, A. Tang, Y. Zhu, and F. Pan, Grain refining and Mechanical Properties of AZ31 Alloy Processed by Accumulated Extrusion Bonding, *J. Alloy. Compd.*, 2018, **745**, p 599–608
44. Y. Yan, W. Deng, Z. Gao, J. Zhu, Z. Wang, and X. Li, Coupled Influence of Temperature and Strain Rate on Tensile Deformation Characteristics of Hot-Extruded AZ31 Magnesium Alloy, Acta Metall, *Sin. Engl.*, 2016, **29**, p 163–172
45. C. Bruni, A. Forcellese, F. Gabrielli, and M. Simoncini, Effect of Temperature, Strain Rate and Fibre Orientation on the Plastic Flow Behaviour and Formability of AZ31 Magnesium Alloy, *J. Mater. Process. Technol.*, 2010, **210**, p 1354–1363
46. S. Spigarelli, O.A. Ruano, M. El Mehtedi, and J.A. Del Valle, High Temperature Deformation and Microstructural Instability in AZ31 Magnesium Alloy, *Mater. Sci. Eng. A*, 2013, **570**, p 135–148
47. A. Fata, G. Faraji, M.M. Mashhadi, and V. Tavakkoli, Hot Deformation Behavior of Mg-Zn-Al Alloy tube Processed by Severe Plastic Deformation, *Arch. Metall. Mater.*, 2017, **62**, p 159–166
48. J.C. Tan and M.J. Tan, Dynamic Continuous Recrystallization Characteristics in Two Stage Deformation of Mg-3Al-1Zn Alloy Sheet, *Mater. Sci. Eng. A*, 2003, **339**, p 124–132
49. T. Al-Samman and G. Gottstein, Dynamic Recrystallization During High Temperature Deformation of Magnesium, *Mater. Sci. Eng. A*, 2008, **490**, p 411–420
50. S.M. Fatemi-Varzaneh, A. Zarei-Hanzaki, and H. Beladi, Dynamic Recrystallization in AZ31 Magnesium Alloy, *Mater. Sci. Eng. A*, 2007, **456**, p 52–57
51. M. Eftekhari, A. Fata, G. Faraji, and M.M. Mashhadi, Hot Tensile Deformation Behavior of Mg-Zn-Al Magnesium Alloy Tubes Processed by Severe Plastic Deformation, *J. Alloy. Compd.*, 2018, **742**, p 442–453
52. J. Deng, Y.C. Lin, S. Li, J. Chen, and Y. Ding, Hot tensile Deformation and Fracture Behaviors of AZ31 Magnesium Alloy, *Mater. Des.*, 2013, **49**, p 209–219
53. D.R. Fang, Z.F. Zhang, S.D. Wu, C.X. Huang, H. Zhang, N.Q. Zhao, and J.J. Li, Effect of Equal Channel Angular Pressing on Tensile Properties and Fracture Modes of Casting Al-Cu Alloys, *Mater. Sci. Eng. A*, 2006, **426**, p 305–313
54. D.R. Fang, Q.Q. Duan, N.Q. Zhao, J.J. Li, S.D. Wu, and Z.F. Zhang, Tensile Properties and Fracture Mechanism of Al-Mg Alloy Subjected to Equal Channel Angular Pressing, *Mater. Sci. Eng. A*, 2007, **459**, p 137–144
55. E.J. Pavlina and C.J. Van Tyne, Correlation of Yield Strength and Tensile Strength with Hardness for Steels, *J. Mater. Eng. Perform.*, 2008, **17**, p 888–893
56. Z. Tang and W. Stumpf, The Effect of Microstructure and Processing Variables on the Yield to Ultimate Tensile Strength Ratio in a Nb-Ti and a Nb-Ti-Mo Line Pipe Steel, *Mater. Sci. Eng. A*, 2008, **490**, p 391–402
57. C.L. Chow, L.G. Yu, and M.Y. Demeri, A Unified Damage Approach for Predicting Forming Limit Diagrams, *ASME J. Eng. Mater. Technol.*, 1997, **119**, p 346–353
58. T. Sakai, A. Belyakov, R. Kaibyshev, H. Miura, and J.J. Jonas, Dynamic and Post-dynamic Recrystallization Under Hot, Cold and Severe Plastic Deformation Conditions, *Prog. Mater Sci.*, 2014, **60**, p 130–207
59. M. Kawasaki, R.B. Figueiredo, and T.G. Langdon, The Flow Characteristics of Superplasticity, *Lett. Mater.*, 2014, **4**, p 78–83
60. T.G. Langdon, Achieving Superplasticity in Ultrafine-Grained Metals, *Mech. Mater.*, 2013, **67**, p 2–8
61. F. Cao, F. Xia, and G. Xue, Hot Tensile Deformation Behavior and Microstructural Evolution of a Mg-9.3Li-1.79Al-1.61Zn Alloy, *Mater. Des.*, 2016, **92**, p 44–57

62. F.D. Dumitru, O.F. Higuera-Cobos, and J.M. Cabrera, ZK60 Alloy Processed by ECAP: Microstructural, Physical and Mechanical Characterization, *Mater. Sci. Eng. A*, 2014, **594**, p 32–39
63. F. Pan, J. Mao, X. Chen, J. Peng, and J. Wang, Influence of Impurities on Microstructure and Mechanical Properties of ZK60 Magnesium Alloy, *T. Nonferr. Metal. Soc.*, 2010, **20**, p 1299–1304
64. W. Yang, X. Guo, and K. Yang, Low Temperature Quasi-Superplasticity of ZK60 Alloy Prepared by Reciprocating Extrusion, *T. Nonferr. Metal. Soc.*, 2012, **22**, p 255–261
65. O. Sabokpa, A. Zarei-Hanzaki, and H.R. Abedi, An Investigation into the Hot Ductility Behavior of AZ81 Magnesium Alloy, *Mater. Sci. Eng. A*, 2012, **550**, p 31–38
66. P.S. Roodposhti, A. Sarkar, and K.L. Murty, Fracture Behavior of AZ31 Magnesium Alloy During Low-Stress High-Temperature Deformation, *Metallogr. Microstruct. Anal.*, 2015, **4**, p 91–101
67. H.J. Frost and M.F. Ashby, *Deformation-Mechanism Maps*, Peragamon Press, Oxford, 1982
68. O.A. Ruano, A.K. Miller, and O.D. Sherby, The Influence of Pipe Diffusion on the Creep of Fine-Grained Materials, *Mater. Sci. Eng.*, 1981, **51**, p 9–16
69. J. Lu, L. Jin, J. Dong, X. Zeng, and W. Ding, Z, Yao, Deformation Behaviors of AZ31 Magnesium Alloy by Equal Channel Angular Extrusion, *T. Nonferr. Metal. Soc.*, 2009, **19**, p 424–432
70. M.Y. Zheng, S.W. Xu, X.G. Qiao, K. Wu, S. Kamado, and Y. Kojima, Compressive Deformation of Mg-Zn-Y-Zr Alloy Processed by Equal Channel Angular Pressing, *Mater. Sci. Eng. A*, 2008, **483–484**, p 564–567
71. J.C. Tan and M.J. Tan, Superplasticity and Grain Boundary Sliding Characteristics in Two Stage Deformation of Mg-3Al-1Zn Alloy Sheet, *Mater. Sci. Eng. A*, 2003, **339**, p 81–89